Article

Accurate and Rapid Extraction of Aquatic Vegetation in the China Side of the Amur River Basin Based on Landsat Imagery

Mengna Chen [1,2], Rong Zhang [2,*], Mingming Jia [2], Lina Cheng [2,3], Chuanpeng Zhao [2], Huiying Li [4] and Zongming Wang [2]

1   School of Land Engineering, Chang'an University, Xi'an 710054, China; 2021135007@chd.edu.cn
2   Key Laboratory of Wetland Ecology and Environment, Northeast Institute of Geography and Agroecology, Chinese Academy of Sciences, Changchun 130102, China; jiamingming@iga.ac.cn (M.J.); chengln23@mails.jlu.edu.cn (L.C.); zhaochuanpeng@iga.ac.cn (C.Z.); zongmingwang@iga.ac.cn (Z.W.)
3   College of Earth Sciences, Jilin University, Changchun 130061, China
4   School of Environmental and Municipal Engineering, Qingdao University of Technology, Qingdao 266520, China; lihy@qut.edu.cn
*   Correspondence: zhangrong@iga.ac.cn

Abstract: Since the early 1950s, the development of human settlements and over-exploitation of agriculture in the China side of the Amur River Basin (CARB) have had a major impact on the water environment of the surrounding lakes, resulting in a decrease of aquatic vegetation. According to the United Nations Sustainable Development Goals, a comprehensive understanding of the extent and variability of aquatic vegetation is crucial for preserving the structure and functionality of stable aquatic ecosystems. Currently, there is a deficiency in the CARB long-sequence dataset of aquatic vegetation distribution in China. This shortage hampers effective support for actual management. Therefore, the development of a fast, robust, and automatic method for accurate extraction of aquatic vegetation becomes crucial for large-scale applications. Our objective is to gather information on the spatial and temporal distribution as well as changes in aquatic vegetation within the CARB. Utilizing a hybrid approach that combines the maximum spectral index composite and Otsu algorithm, along with the integration of convolutional neural networks (CNN) and random forest, we applied this methodology to obtain an annual dataset of aquatic vegetation spanning from 1985 to 2020 using Landsat series imagery. The accuracy of this method was validated through both field investigations and Google Images. Upon assessing the confusion matrix spanning from 1985 to 2020, the producer accuracy for aquatic vegetation classification consistently exceeded 87%. Further quantitative analysis unveiled a discernible decreasing trend in both the water and vegetation areas of lakes larger than 20 km^2 within the CARB over the past 36 years. Specifically, the total water area decreased from 3575 km^2 to 3412 km^2, while the vegetation area decreased from 745 km^2 to 687 km^2. These changes may be attributed to a combination of climate change and human activities. These quantitative data hold significant practical implications for establishing a scientific restoration path for lake aquatic vegetation. They are particularly valuable for constructing the historical background and reference indices of aquatic vegetation.

Keywords: aquatic vegetation; spatial distribution; CNN; random forest

1. Introduction

Lakes serve as crucial links in the interaction of various elements within terrestrial ecosystems [1–3]. They fulfill diverse ecological functions, including the regulation of river runoff and the breeding of aquatic organisms, and play a significant strategic role in safeguarding national social and economic interests, and ecological security [4–6]. Aquatic vegetation is a crucial component of lake ecosystems, and its degradation and loss serve as important indicators of ecosystem decline in lakes [7,8]. It also plays a crucial role in maintaining the balance of lake ecosystems by stabilizing sediments, sequestering carbon,

improving water quality, facilitating nutrient cycling, and providing food and habitat for a variety of aquatic organisms [9–12]. Aquatic vegetation can be categorized into three types based on its position relative to the water surface: emergent vegetation, floating-leaved vegetation, and submerged vegetation [13].

The Amur River Basin, spanning Russia, China, and Mongolia, ranks among the ten largest river basins in the world [14]. The Chinese part of the basin constitutes 48% of the entire basin and hosts the majority of freshwater lakes in Northeast China. It stands as the region with the most abundant water resources and densest concentration of lakes in Northeast China. Additionally, it boasts the largest natural forest area and serves as a crucial commercial grain base in China [15,16]. More than 93% of the population of the entire basin lives on the China side of the Amur River Basin (CARB) [17]. Since the early 1950s, the development of human settlements and agriculture in the CARB has significantly impacted the region's natural wetlands [18,19]. The excessive use of groundwater, fertilizers, pesticides, and other agricultural inputs, along with the overdevelopment of agriculture, has resulted in the degradation of cultivated land and the serious pollution of wetlands. These practices have had a significant impact on the aquatic environment of the surrounding lakes [20]. This has led to the decline of aquatic vegetation in the lakes, significantly affecting the living environment quality of the surrounding residents. Moreover, it causes negative impacts on the effective utilization of water supply resources and hampers social and economic development. A comprehensive understanding of temporal and spatial changes in aquatic vegetation within the basin is indispensable to assessing ecosystem services and supporting the sustainable conservation of the region's wetlands.

Traditional methods of monitoring aquatic vegetation rely on labor-intensive field surveys, making it challenging to obtain continuous spatial distribution information. As a non-contact detection method, remote sensing has unique advantages in the monitoring and extraction of aquatic vegetation information [21]. In general, satellite remote sensing data with varying resolutions can achieve an overall accuracy of aquatic vegetation group classification above 80% [22]. However, due to the influence of water and other environmental factors, the radiation transfer mechanism of the aquatic vegetation canopy becomes highly complex, thereby increasing the difficulty of its accurate identification. In recent years, various classification methods have been applied to monitor changes in aquatic vegetation. For example, Jing et al. used micro unmanned aerial vehicle images to generate visible vegetation indices, establish decision tree rules, and automatically classify the ecological area of the Xin Cheng Waterside Forest Park in Beijing, achieving an overall accuracy of 91.7% [23]. Chen et al. proposed a new concave–convex decision function for detecting submerged aquatic vegetation (SAV) in Lake Ulansuhai, with classification accuracies of 92.17% and 91.79% for July and August, respectively [24]. Wang et al. first proposed an enhanced aquatic vegetation index based on the difference in two short-wave infrared (SWIR) bands to extract the aquatic vegetation above the water surface. Subsequently, using Taihu Lake as an example, they accurately extracted seasonal and annual distributions of aquatic vegetation [25]. Ashford described a field investigation method and image processing workflow based on unmanned aerial systems (UAS), which was used to map local, exotic, and invasive aquatic vegetation, indicating that small UAS can investigate, map, and detect features of interest in a large area [26]. Additionally, machine learning methods, including random forest (RF) classification and deep learning, have also been employed [27–29], demonstrating significant potential in the field of aquatic vegetation extraction. Aquatic vegetation extraction based on deep learning achieves precise identification by learning features from a large amount of remote sensing image data. Therefore, deep learning technology provides new insights and approaches for aquatic vegetation extraction. The results of Ji et al. indicated that the integration of CNN and RF classifiers slightly outperforms independent RF classification and CNN classification methods in terms of classification accuracy [30]. However, there is currently a lack of research on integrating CNN and RF classifiers for aquatic vegetation information extraction.

The specific objectives of this study are as follows: (1) to propose a novel and robust classification method by integrating image composite algorithms, CNN, and RF classifiers; (2) to apply the proposed method to generate annual maps of aquatic vegetation, water, and other land cover types in the CARB from 1985 to 2020; (3) to analyze the spatiotemporal changes of aquatic vegetation, water, and other land cover types during the period of climate change from 1985 to 2020. This study extends the spatial transferability of the model and provides strong methodological and theoretical support for future extraction and monitoring of aquatic vegetation.

2. Materials and Methods

2.1. Study Area

As shown in Figure 1, the CARB (41°45′–53°33′N, 115°13′–135°05′E) encompasses most of Heilongjiang and parts of Jilin and Inner Mongolia. We selected the China side of the Amur River Basin with lakes larger than 20 km^2 as the study area. The basin has a monsoon climate, with winds alternating between continental and maritime with the seasons. The summer is short, warm, and humid, with temperatures ranging from 16–18 °C in July. The winter is long (November to March), dry, and cold, and January is the coldest month, with temperatures ranging from −31 to −15 °C. Nearly two-thirds of the basin's precipitation occurs from June to August. The peak period of vegetation biomass in the study area occurs from July to August, while the ice cover period lasts from November to March the following year. The average annual temperature ranges from −8 to 6 °C, and the average annual precipitation ranges from 250 to 800 mm. The area exhibits abundant water resources and diverse flora and fauna, making it a significant ecological hotspot. The aquatic vegetation types of the CARB are mainly reed communities, wild barley communities, *Potamogeton wrightii* Morong communities, *Calamagrostis epigeios* (L.) Roth communities, *Suaeda salsa* communities, *Zizania latifolia* (Griseb.) Turcz. ex Stapf communities, Typha orientalis Presl communities, and so on. Moreover, over the past three decades, it has thrived as an agricultural region, particularly renowned for its prominent role in rice cultivation.
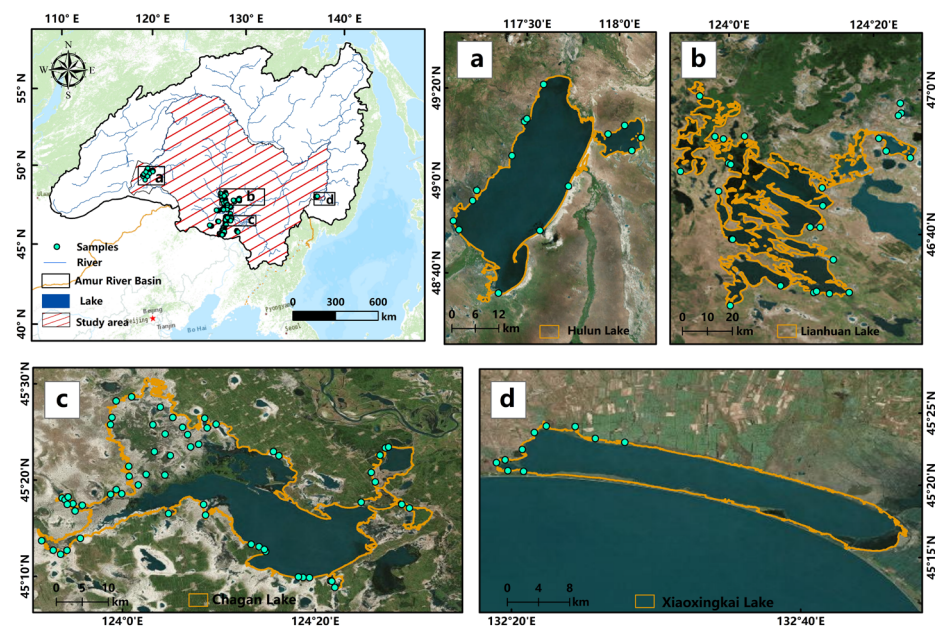

Figure 1. Location of the study area. (**a**) Hulun Lake, (**b**) Lianhuan Lake, (**c**) Chagan Lake, (**d**) Xiaoxingkai Lake.

2.2. Remote Sensing Data

The Landsat series, initially launched in 1972, has a 16-day revisit period and a spatial resolution of 30 m. Due to the limited availability of Landsat-4 TM satellite imagery in China, this study utilized surface reflectance data from Landsat-8 OLI, Landsat-7 ETM+, and Landsat-5 TM. The Scan Line Corrector (SLC) of the Landsat-7 ETM+ sensor failed after 2003, resulting in striping gaps in Landsat-7 image data. This study utilized Landsat-7 ETM+ data from 1999 to 2002. For 2012, only Landsat-7 ETM+ satellite imagery was available, which required banding correction before use. A total of 6175 Landsat surface reflectance images were selected from the Google Earth Engine (GEE) data catalog for the period between 1985 and 1 June 2020, with a focus on the dates from 15 May to 15 October. The temporal distribution of the Landsat satellite series used in this study and the effective observation quantity of Landsat-8 satellite in 2020 are shown in Figure 2.
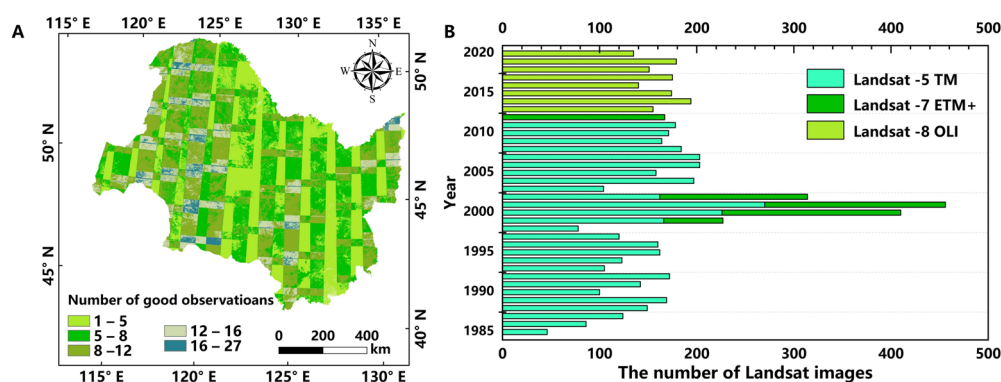

Figure 2. Spatial distribution and the number of good observations across the CARB in 2020 by Landsat-8 OLI (**A**) and number of Landsat images used in the study (**B**).

2.3. Ground Sample Data

The validation data used in this study consisted of 286 field survey samples, high-resolution images obtained from Google Earth, and high-resolution images from national geographic monitoring. The labelme tool was employed for manual visual interpretation to create a labeled dataset of 1200 images with pixels of 128 × 128, which included water surfaces, aquatic vegetation (emergent vegetation, floating-leaved vegetation, and submerged vegetation), and other surface features such as muddy areas in lake transition zones and terrestrial vegetation. In this dataset, 70% of the labels were used for training, while 30% of the samples were reserved for validating the accuracy of the classification results.

2.4. Methodologies

2.4.1. Basic Idea

The mapping workflow for aquatic vegetation, water, and other land cover types (including inland vegetation, algal blooms, agricultural fields, bare soil, built-up areas, etc.) in the CARB is illustrated in Figure 3. Firstly, we utilized the Landsat imagery along with image composite (the specified band value of each pixel at all pixel positions in the image stack is sorted pixel by pixel, maximum value, mean value, or median value, etc., of the specified band are extracted, and finally, all these pixels are formed into an image) and Otsu algorithm (Otsu) to delineate the maximum spatial extent of water surfaces of large lakes (larger than 20 km^2) in the CARB. Subsequently, we developed a novel and robust classification method by combining the image composite, CNN, and RF classifier. This classification approach consists of three steps: (1) obtaining a synthesized image collection of the CARB lakes from high-quality observational data; (2) extracting features from the image collection using a CNN model; (3) classifying the extracted CNN features using an RF classifier.
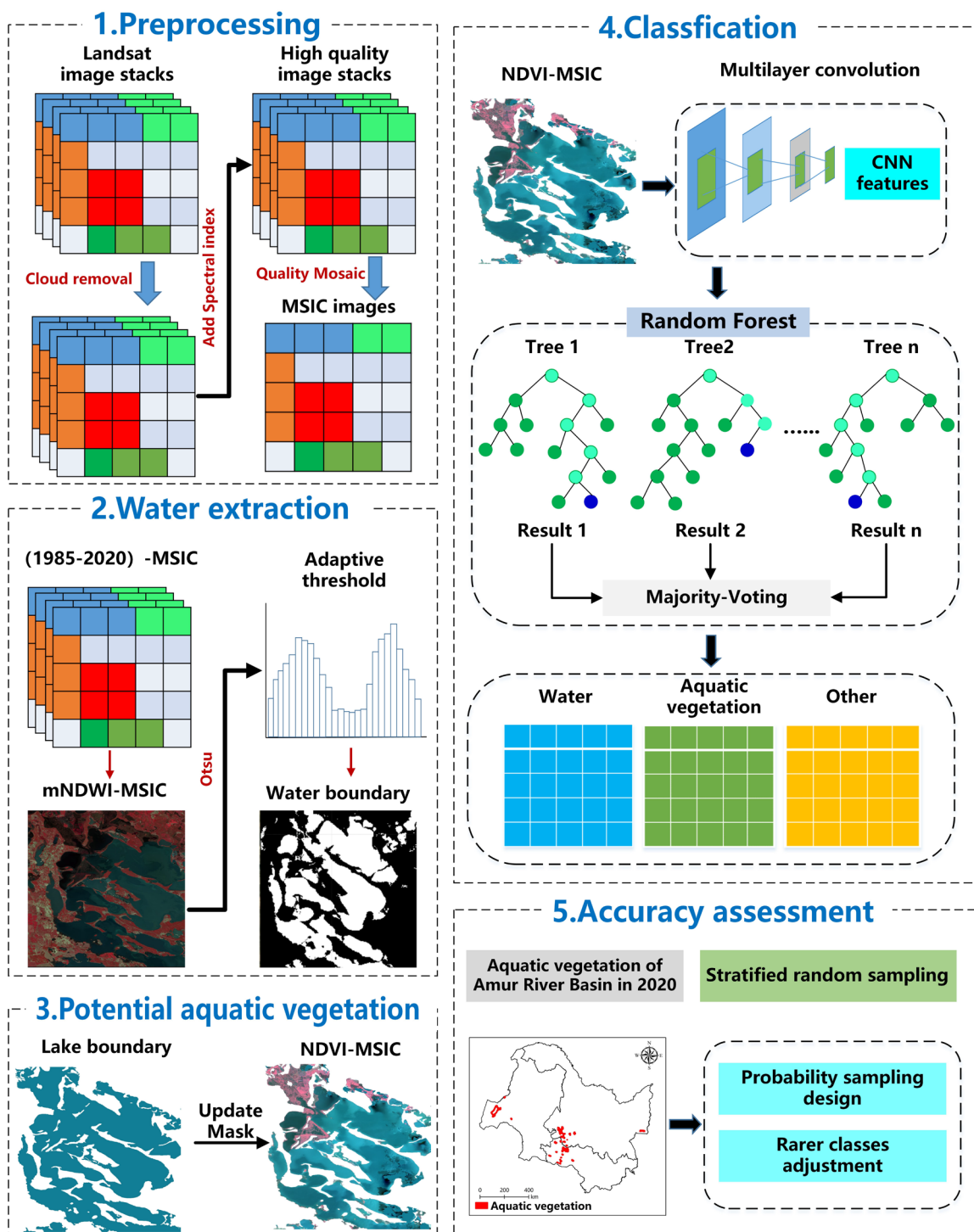
Figure 3. Technical roadmap of aquatic vegetation extraction.

2.4.2. The Maximum Spectral Index Composite (MSIC) and Otsu

The GEE API offers the "imageCollection.qualityMosaic" function, which utilizes a maximum spectral index composite (MSIC). The MSIC algorithm selects a specified band as a sorting criterion on a pixel-by-pixel basis. It then computes the maximum value after sorting the pixels based on this criterion. The quality measure band is used as the primary source for each pixel in the final composite image, where the pixel values are obtained by overlaying the specified band data. This approach ensures that the resulting composite image showcases the highest quality pixels, which are defined as the pixels with

the maximum spectral index selected at each pixel position in the time series image stack after cloud removal, based on the selected band. The Otsu, also referred to as the maximum inter-class variance method, was proposed by Otsu in 1975 [31] and has been further studied [32]. This algorithm divides an image into two parts, distinguishing between the background and foreground based on the grayscale characteristics of the image. The optimal threshold is determined by selecting the threshold that maximizes the inter-class variance and minimizes the in-class variance which is then applied for automatic binary classification of the image, enabling efficient segmentation.

2.4.3. Spectral Feature Construction

This study relies on the GEE platform to construct spectral features and enhance the extraction of aquatic vegetation information. These feature variables have been carefully selected and integrated to provide comprehensive and reliable analysis of aquatic vegetation. The spectral index formulas used in this study are shown in Table 1.

Table 1. Formulas of the spectral indices used in this study.

Spectral Name	Expression	Source
NDVI (Normalized Differential Vegetation Index)	$NDVI = \frac{NIR - Red}{NIR + Red}$	[33]
mNDWI (Modified Normalized Difference Water Index)	$mNDWI = \frac{Green - SWIR}{Green + SWIR}$	[34,35]
FAI (Floating Algae Index)	$FAI = (NIR - Red - (SWIR - Red) \times \frac{(\lambda NIR - \lambda Red)}{(\lambda SWIR - \lambda Red)}$	[36]

NIR represents Near-Infrared band Reflectance; Red represents infrared band reflectance; *SWIR* represents Short-Wave Infrared band reflectance; Green represents green band reflectance; λNIR, λRed, and $\lambda SWIR$ are the center wavelengths of the near-infrared, red, and shortwave infrared bands, respectively.

2.4.4. Delineating Spatial Extents of Lakes in the CARB

According to research conducted by Jia et al. [35], the mNDWI (Modified Normalized Difference Water Index) effectively enhances the distinction between artificial shorelines, such as embankments, roads, and pond edges, and the surrounding water. It outperforms the NDWI (Normalized Difference Water Index) in extracting intertidal zones and inland surface water coverage. Therefore, this study selected mNDWI for the extraction of lake water. In this study, the MSIC synthetic image was constructed annually using the mNDWI, and the maximum water surface image was generated. The OA was applied to select the threshold for mNDWI, facilitating the determination of the maximum water surface range on a yearly basis. Subsequently, these ranges were merged to obtain the maximum coverage of lake water surfaces within the study area from 1985 to 2020.

2.4.5. Convolutional Neural Network (CNN)

CNN, proposed by Lecun et al. in the late 1980s [37], is a deep learning model primarily used for image recognition and computer vision tasks. The principle consists of the following key concepts: (1) Convolutional Layer: The convolutional layer is a core component of CNN. It extracts the features of the image by convolution operations on the input image using a series of learnable filters, or convolution nuclei. Each filter slides over the image and calculates the inner product of its corresponding local receptive field, generating a Feature Map. Through the combination of multiple filters, the convolution layer can learn different features, such as edges, textures, etc. (2) Pooling Layer: the pooling layer is used to downsample the feature map, reduce the size and number of parameters of the feature map, and retain the main features. Common pooling operations include Max Pooling and Average Pooling, which select the maximum value or average value of the experience field, respectively, as the pooled value. (3) Activation Function: The activation function introduces nonlinear transformations that enable the CNN to learn nonlinear features. Common activation functions include Rectified Linear Unit (ReLU), Sigmoid, and Tanh. (4) Fully Connected Layer: The fully connected layer flattens the output

of the convolutional layer and the pooling layer and fully connects it with the previous layer to convert the extracted feature map into the output of classification or regression. Fully connected layers typically use a Multi-Layer Perceptron (MLP) structure. (5) Back propagation: Forward propagation and back propagation are interdependent processes. Forward propagation calculates and stores the results of each layer of the neural network from the input layer to the output layer in turn. On the other hand, back propagation uses chain rule to calculate the gradient of loss function relative to the weight of each layer, so as to update the weight to minimize the loss function. Loss function plays a key role in the training process by measuring the difference between the predicted results of the model and the actual tags. Through back propagation, CNN can gradually extract the abstract features of the image and automatically learn more advanced feature representations during the training process.

The CNN structure adopted in this study is shown in Figure 4. The network structure of DeepPlabv 3+ is used to extract features [38]. The model is trained with labeled data sets. The main body of its encoder is the DCNN feature extraction network with atrous convolution, and the Xception_65 network structure and Xception_71 network structure are selected. DeepPlabv3+ introduces atrous spatial pyramid pooling (ASPP) to fuse context information at different scales. The ASPP module includes several parallel branches of atrous convolution. Each branch has a different dilation rate. In this way, rich contextual information can be captured at different scales and fused into the segmentation results. The decoder fuses the features of the bottom layer and the top layer by techniques such as upsampling and skip connections, and the extracted CNN features are used as the input of the random forest classifier.
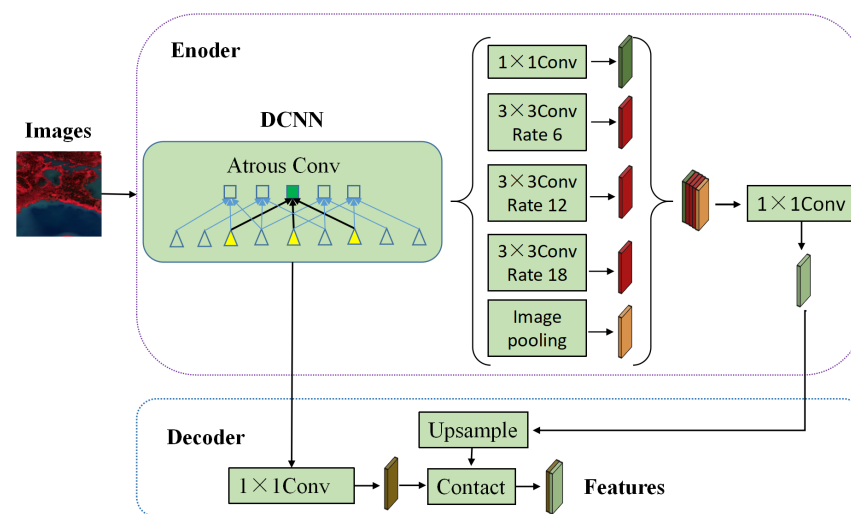

Figure 4. Network structure of CNN feature extraction.

2.4.6. Random Forest (RF) Classification Algorithm

RF is an ensemble learning algorithm known for its advantages, including insensitivity to multivariate collinearity, no requirement for data normalization, and good tolerance for missing and unbalanced data [39]. RF is an integrated method consisting of classification trees and regression trees. The final classification decision is determined by averaging the probabilities of class assignments computed across all generated trees [40]. There are two random processes in RF. First, a training set is created for each tree by sampling replacements from the original training data set. Second, when the nodes of the tree are split, random features are selected from the total features without replacement. RF has been widely adopted because it can improve the robustness and performance of classification based on bootstrap sampling and random feature combination strategies [41]. In addition, it can process multiple variables, rank them, assess variable importance based on performance, and determine the computationally optimal number of trees through

algorithm testing. Moreover, RF can overcome the overfitting problem of decision trees and exhibits strong resilience to noise and outliers.

2.4.7. Accuracy Assessment

In this study, a confusion matrix was constructed to obtain the Kappa coefficient, Overall Accuracy (OA), Producer Accuracy (PA), and User Accuracy (UA). OA expresses the overall degree of agreement in the matrix. UA represents the likelihood that a classified object matches the ground situation. PA shows the percentage of an object type, which was correctly classified. Kappa coefficient states how well the classification results agree with the reference data. The formulas are shown in Table 2.

Table 2. Formulas of overall accuracy, Kappa coefficient, producer accuracy, and user accuracy.

Evaluation Index	Equation	Description
Overall Accuracy	$OA = \frac{\sum\limits_{i=1}^{k} X_i}{N}$	The ratio of correctly classified category pixels to total category pixels
Kappa coefficient	$Kappa = \frac{OA-P}{1-P}$ $P = \frac{1}{N^2}\left(\sum\limits_{i=1}^{m} X_i \bullet \sum\limits_{i=1}^{r} X_i\right)$	Used to evaluate the consistency of classification results
Producer Accuracy	$PA = \frac{X_i}{\sum\limits_{i=1}^{m} X_i}$	The ratio of the number of correctly classified pixels of a class to the total number of true reference pixels of that class
User Accuracy	$UA = \frac{X_i}{\sum\limits_{i=1}^{r} X_i}$	The ratio of the number of correctly classified pixels of a class to the total number of pixels of that class

3. Results

3.1. Accuracy Assessment

Table 3 presents the comprehensive confusion matrix for the classification results in 2020. The OA of the land cover map reached 90.6%. The UA for aquatic vegetation and water was 91.07% and 90.91%, respectively, while the UA for other land cover types was 89.29%. Notably, the OA for aquatic vegetation and other land cover types fell below 90%, although the highest PA for water reached 93.75%. When assessing the confusion matrix from 1985 to 2020, the PA of the land cover maps consistently exceeded 87%. The evaluation, conducted through confusion matrix calculations, indicated strong agreement between the obtained maps and ground measurement points.

Table 3. Classification confusion matrix and precision analysis in 2020.

Class	Aquatic Vegetation	Water	Other	Total	UA
Aquatic vegetation	51	2	3	56	91.07%
Water	3	30	0	33	90.91%
Other	3	0	25	28	89.29%
Total	57	32	28	117	
PA	89.47%	93.75%	89.29%		
OA	90.60%	Kappa	85.13%		

3.2. Analysis of the Spatial–Temporal Changes of the Overall Water and Aquatic Vegetation in the Study Area

The overall lake changes are shown in Figure 5. Aquatic vegetation fluctuated greatly during 1985–2001, showing an overall increasing trend, rising from 745 km^2 to 851 km^2. Aquatic vegetation showed a decreasing trend from 2001 to 2003, reducing from 851 km^2 to 596 km^2. The change in aquatic vegetation remained relatively stable from 2004 to 2019, with a significant increase observed in 2020. The overall water surface of the CARB

shows a shrinking trend. Water surface showed a slight increasing trend from 1985 to 1987, rising from 3575 km^2 to 3775 km^2, a slight decreasing trend from 1988 to 1989, from 3671 km^2 to 3619 km^2, and a small increasing trend from 1990. By 1997, water surface was in a relatively stable state. Due to artificial intervention, water surface showed an overall decreasing trend from 1998 to 2012, reducing from 3795 km^2 to 2902 km^2. To promote the integrated protection and restoration of mountains, rivers, forests, fields, lakes, grasslands, and deserts, a series of fundamental, pioneering, and long-term efforts has been undertaken. Water surface showed a small decline from 2013 to 2018, gradually recovering after 2019. From 1997 to 2011, other land use classes increased sharply from 349 km^2 to 1135 km^2. With population growth and economic development, the demand for food, agricultural products, and construction also increased, causing people to sacrifice part of the water surface and aquatic vegetation to meet the needs of development. By 2013, it dropped sharply to 612 km^2. From 2014 to 2018, the area of other landincreased. However, by 2020 other land area reduced to 522.4 km^2.
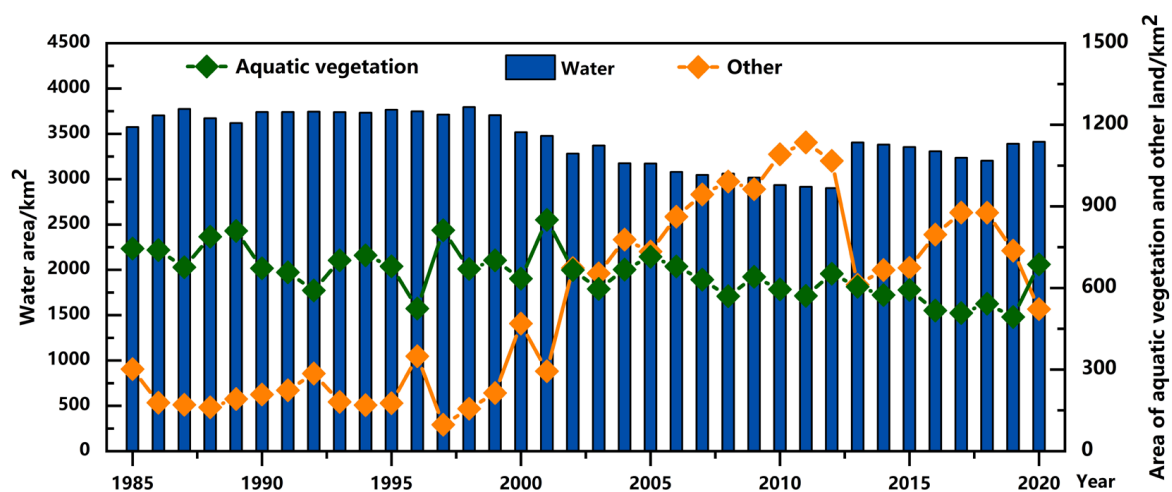

Figure 5. Changes in total aquatic vegetation and water area of the whole study from 1985 to 2020.

The changes in the main lakes (Hulun Lake, Lianhuan Lake, Chagan Lake and Xiaoxingkai Lake) are shown in Figure 6. Aquatic vegetation showed a slight decreasing trend from 1985 to 1987, from 486 km^2 to 485 km^2, and began to increase in 1988. In 1989, the aquatic vegetation was relatively stable, with an area of 549 km^2, and then it showed a decreasing trend. In 1992, aquatic vegetation area was 332 km^2, and during 1992–1996 it showed a fluctuating trend. In 1996, the aquatic vegetation area was 315 km^2, and this increased to 477 km^2 in 1997. From 1997 to 2006, aquatic vegetation fluctuated in a small range. In 2006, the aquatic vegetation area was 340 km^2, and during 2006–2020, the area of aquatic vegetation was relatively stable. In 2020, the area of aquatic vegetation was 428 km^2. Overall, the change trend of water surface and other land in these four typical lakes is close to that in all the lakes as a whole.
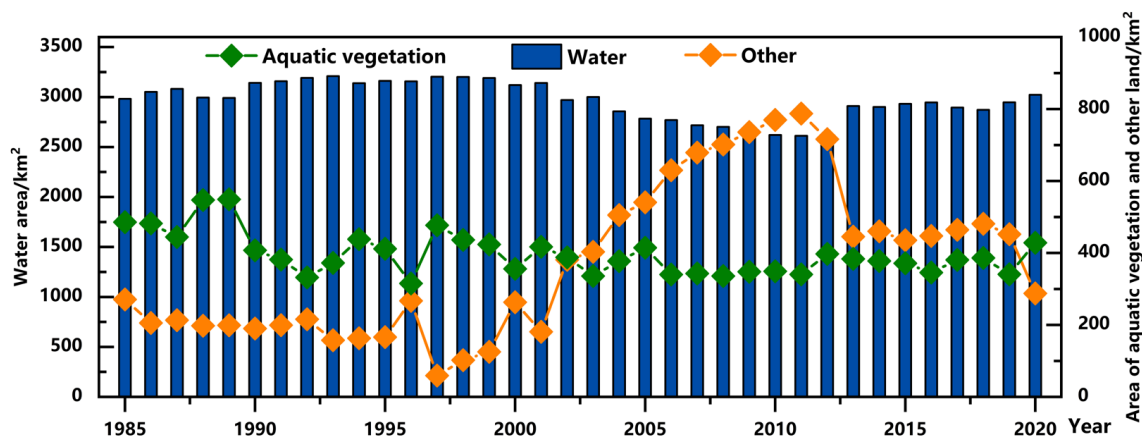
Figure 6. Changes in aquatic vegetation and water area of Hulun Lake, Lianhuan Lake, Chagan Lake, and Xiaoxingkai Lake from 1985 to 2020.

3.2.1. Temporal and Spatial Changes of Aquatic Vegetation in Hulun Lake

As depicted in Figure 7, aquatic vegetation in Hulun Lake is primarily concentrated in the south, southwest, and northeast, typically growing at the lake's edge. From 1985 to 1989, there was a continuous increase in aquatic vegetation, while the lake area remained relatively stable. In 1990, the water area started to increase, whereas aquatic vegetation began to decrease, indicating a decline in the water quality of the lake. The area of water and aquatic vegetation was relatively stable from 1990 to 2001, steadily decreased from 2002 to 2010, remained stable from 2011 to 2013, and showed a steady increase from 2014 to 2020. The overall water changes in Hulun Lake were predominantly concentrated in the eastern, northeastern, southern, and southeastern parts of the lake, while other locations remained relatively stable. The most dramatic changes occurred in the northeast part of the lake, where the lake area expanded significantly in 1990 and remained stable until 2001. However, the water surface in the region experienced a dramatic shrinkage in 2005 and complete drying between 2006 and 2019. Nevertheless, in 2020, water began to reappear in this area, leading to a significant increase in aquatic vegetation. From 2002 to 2020, the overall aquatic vegetation in Hulun Lake exhibited slight fluctuations but demonstrated an overall increasing trend.

3.2.2. Temporal and Spatial Changes of Aquatic Vegetation in Lianhuan Lake

As depicted in Figure 8, aquatic vegetation around the lake is primarily concentrated in the northern part, with a small amount distributed along the lake boundary. From 1985 to 1989, the water surface of the lake remained relatively stable. It exhibited an increasing trend in 1990, gradually decreased from 1991 to 1995, and then increased again in 1996. The area of the water surface initially decreased from 1996 to 2001 and then increased. However, in 2002, the water surface significantly shrank. Subsequently, from 2003 to 2013, the water surface increased steadily, followed by a period of decline from 2014 to 2018. Notably, there was an upward trend from 2017 to 2020. The most significant changes occurred in the northeastern part of the lake. From 1985 to 1989, the surface area of aquatic vegetation increased slightly. From 1989 to 1996, it first decreased slightly and then increased. In 1997, the surface area of aquatic vegetation increased significantly. In 1998, there was a slight increase, but in 1999, the surface area of aquatic vegetation began to decrease sharply. It maintained a relatively stable state in 2001, steadily increased from 2002 to 2005, and then gradually decreased from 2006 to 2013. From 2014 to 2020, the water vegetation area exhibited a pattern of initially increasing and then decreasing. Generally speaking, the aquatic vegetation area showed a decline from 1985 to 2020. Strengthening the protection and restoration of aquatic vegetation in lakes is essential.
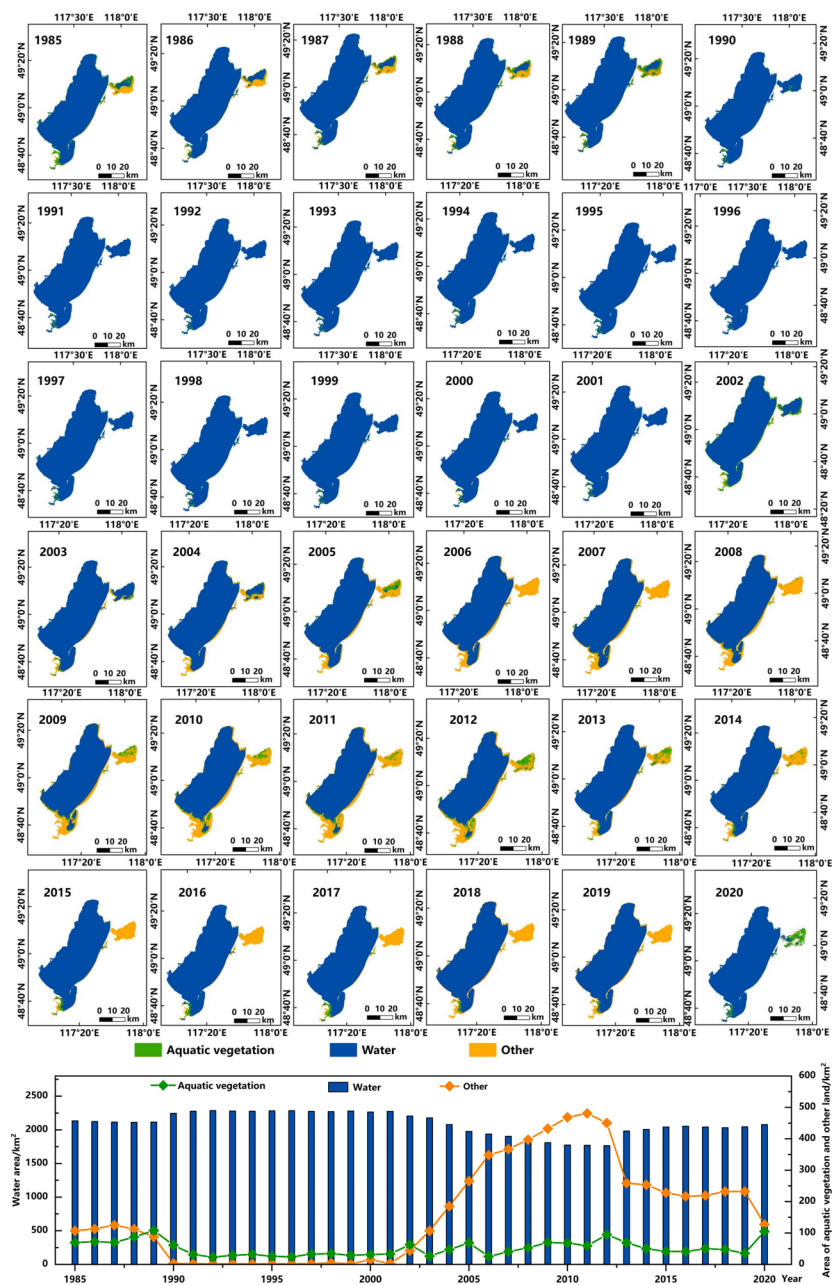
Figure 7. Spatial and temporal distribution and area changes of aquatic vegetation and water of Hulun Lake from 1985 to 2020.
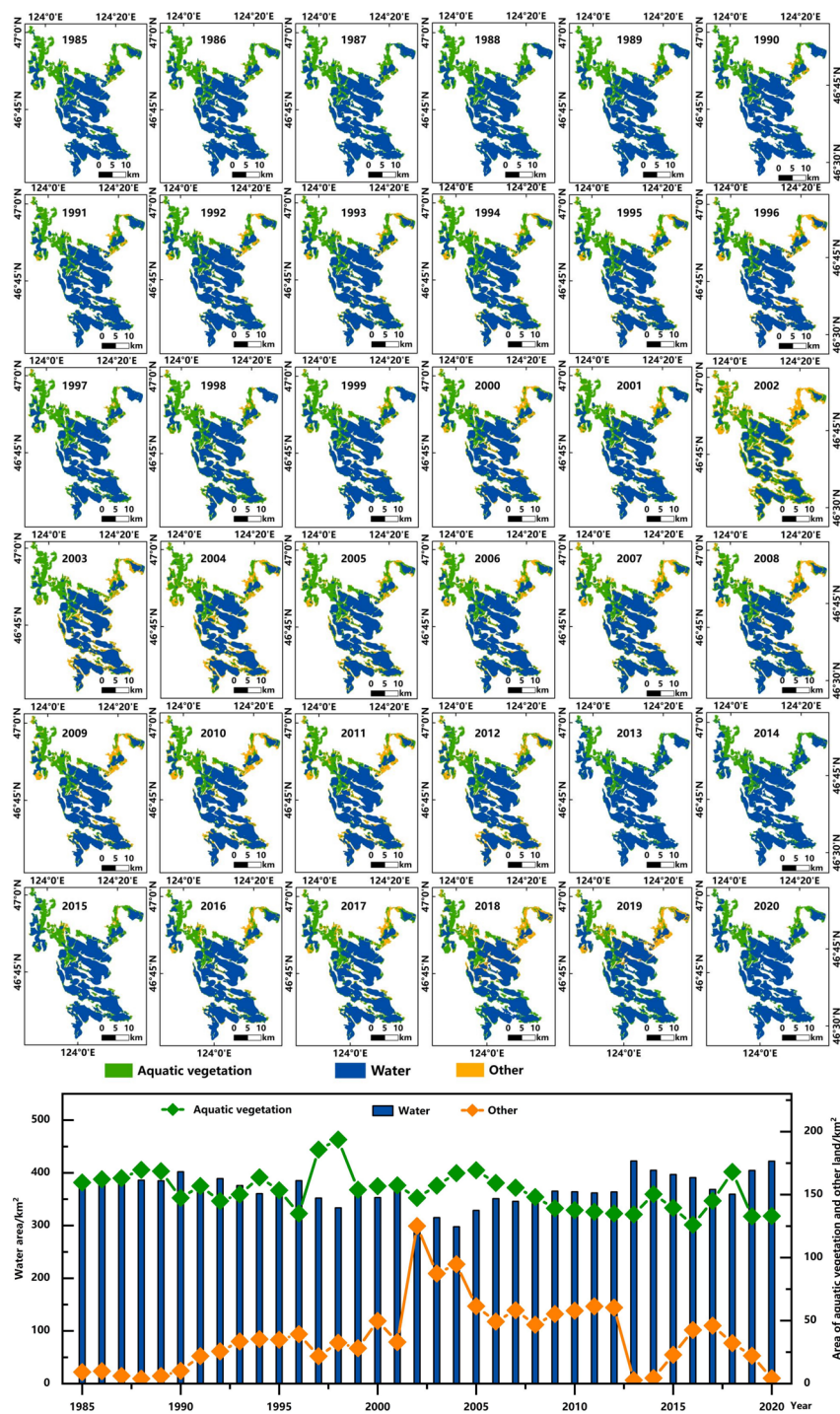
Figure 8. Spatial and temporal distribution and area changes of aquatic vegetation and water of Lianhuan Lake from 1985 to 2020.

3.2.3. Temporal and Spatial Changes of Aquatic Vegetation in Chagan Lake

As shown in Figure 9, aquatic vegetation in Chagan Lake is primarily concentrated in the northwestern and northeastern regions. The water surface of Chagan Lake increased significantly from 1985 to 1987 and decreased from 1987 to 1990. The lake surface area increased from 1988 to 1993, started to decrease from 1994 to 1996, and experienced a sharp increase in 1997–1998. From 1999 to 2002, the lake area steadily decreased, and from 2003 to 2020, it exhibited little fluctuation, remaining essentially stable. The primary reason for the change in the overall water surface of Chagan Lake is the transformation occurring

in the northwest part of the lake, while other areas remain relatively stable. From 1985 to 2020, the aquatic vegetation area of Chagan Lake exhibited significant fluctuations. It decreased from 1985 to 1987, followed by a notable increase in 1988. The aquatic vegetation area decreased from 1988 to 1992, increased from 1992 to 1994, and remained stable from 1994 to 1995. There was a significant decrease in the area of aquatic vegetation in 1996. Subsequently, the area fluctuated greatly from 1996 to 2001 and showed a downward trend from 2001 to 2008. However, the aquatic vegetation area increased in 2005 and continued to rise from 2008 to 2020.
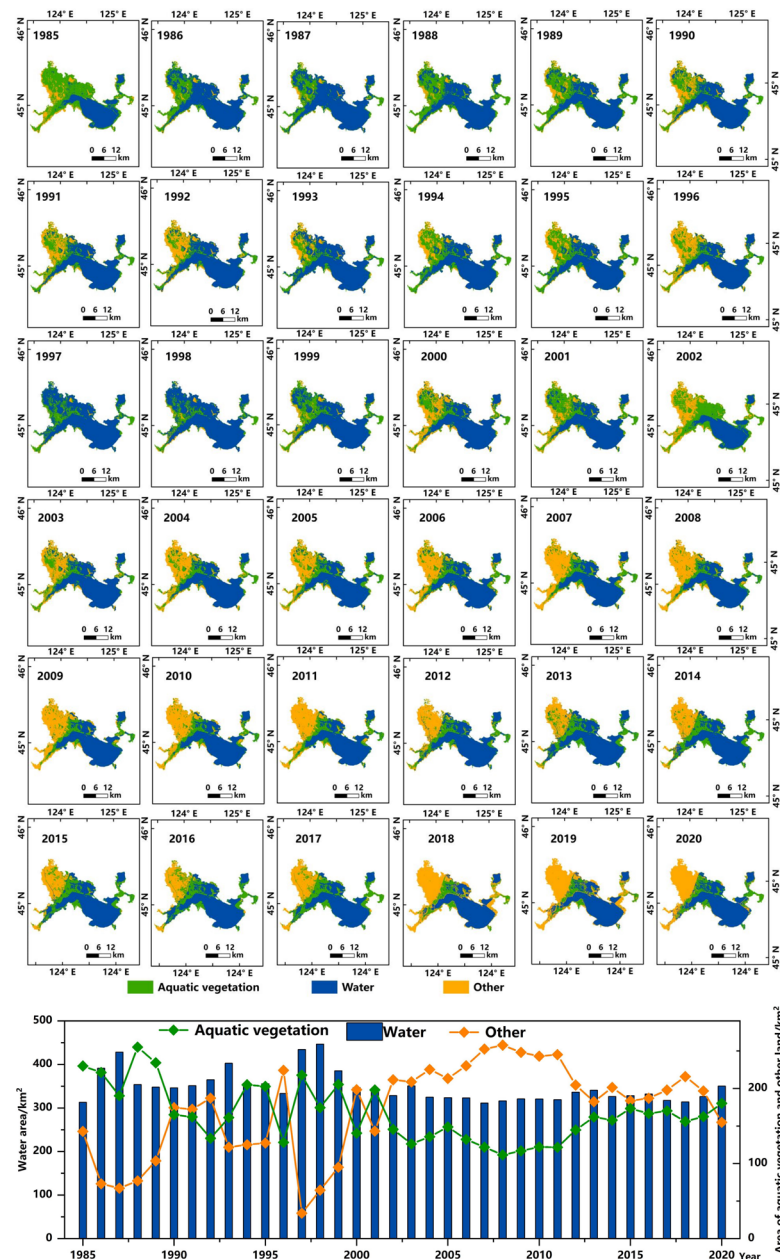

Figure 9. Spatial and temporal distribution and area changes of aquatic vegetation and water of Chagan Lake from 1985 to 2020.

3.2.4. Temporal and Spatial Changes of Aquatic Vegetation in Xiaoxingkai Lake

As shown in Figure 10, aquatic vegetation in Xiaoxingkai Lake is primarily concentrated in the eastern and southeastern parts, with a smaller amount distributed near the lake boundary. According to the statistical chart depicting the water and aquatic vegetation

area of Xiaoxingkai Lake from 1985 to 2020, it is evident that the surface of Xiaoxingkai Lake exhibited an overall growth trend during this period. Specifically, from 1985 to 2002, the surface experienced slight fluctuations but remained relatively stable. Subsequently, from 2002 to 2020, the lake surface area showed a steady and gradual increase. In terms of the aquatic vegetation area, significant fluctuations were observed in Xiaoxingkai Lake from 1985 to 2020. Initially, there was a decrease in the aquatic vegetation area from 1985 to 1987, followed by a substantial increase from 1988 to 1990. The aquatic vegetation area experienced a continuous decrease from 1990 to 1992. However, from 1992 to 1997, the area exhibited a pattern of first increasing, then decreasing, and then increasing again. Finally, from 1997 to 2020, there was a consistent trend of decreasing aquatic vegetation area.
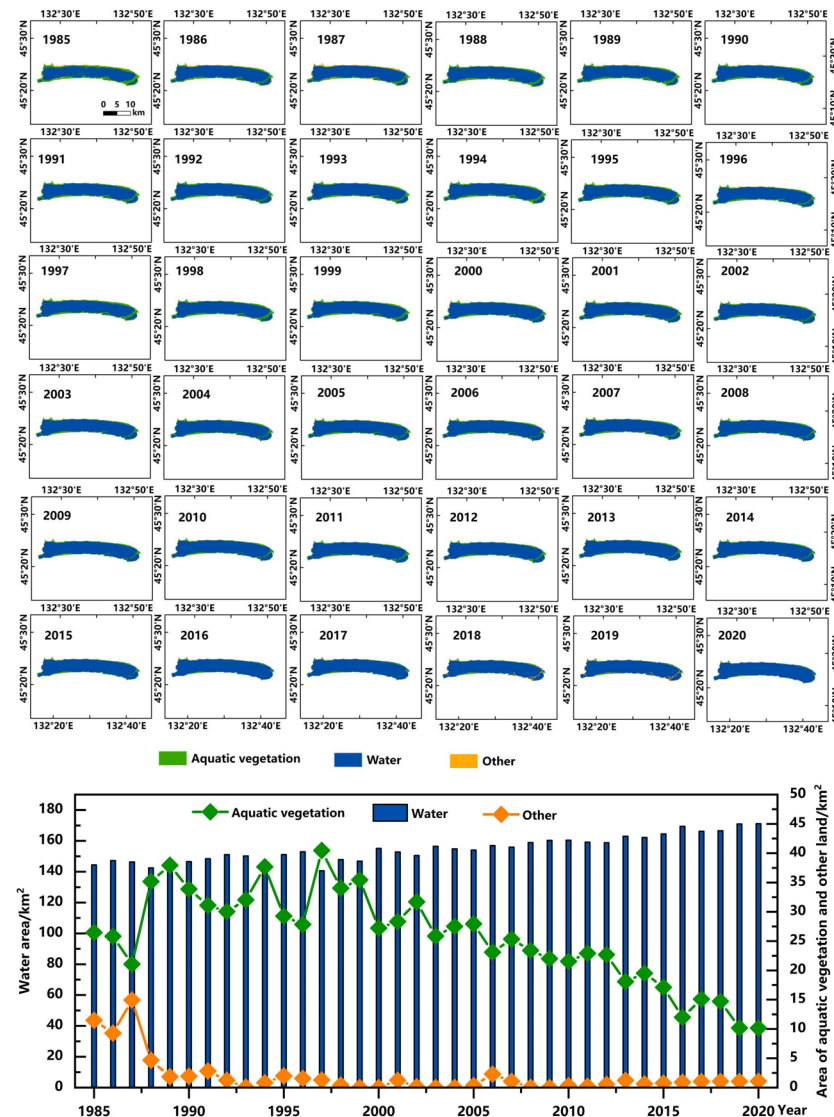

Figure 10. Spatial and temporal distribution and area changes of aquatic vegetation and water of Xiaoxingkai Lake from 1985 to 2020.

4. Discussion

4.1. The Advantages of the Model in Large-Scale Extraction of Aquatic Vegetation

In this study, a MSIC-Otsu and CNN-RF classifier method were developed to accurately extract aquatic vegetation. The maximum water surface boundary of the lake and the maximum coverage area of aquatic vegetation were determined by the time series Landsat images on the GEE platform and MSIC-Otsu. The CNN-RF classifier was used to extract the distribution of aquatic vegetation, water, and other land covers. The successful

implementation of this study can be mainly attributed to three factors: the availability of a large number of free Landsat images, the powerful parallel computing capability of the GEE platform, and the robust MSIC-Otsu and CNN-RF methods. GEE can rapidly access and process a large volume of Landsat imagery without the need for additional masking or extensive pre-processing and post-processing steps. In CNN, the classifier consists of a fully connected layer, and the final decision criterion is based on calculation accumulation and activation. The advantage of CNN lies in its ability to directly extract more representative and abstract features from the original data [42–44]. This includes extracting texture information of different types of land use in remote sensing images, shape features such as boundary shape, geometric shape, and contour shape, spectral features encompassing spectral reflectance, spectral intensity, and spectral features, context features referring to the spatial relationship of surrounding pixels to infer the features of the target, and multi-scale features obtained through multi-layer convolution and pooling operations to capture information at different scales in remote sensing images. Li et al. used the open source dataset DeepSat to build and test the CNN model. The results proved that the CNN model was effective in land use classification and CNN did have the learning ability to extract the most critical and effective information from the training dataset [45]. Ståhl et al. used deep CNN to identify wetland areas in historical maps using deep convolutional neural networks. The presented deep CNN performs well [46]. As a more complex and reliable classifier, the RF classifier has been proven to achieve superior classification performance through strategies such as boosting and bagging [47,48]. Aiming at the problem of image classification and recognition, Xi proposed a hybrid model based on CNN, and input the features extracted by CNN into RF for classification. The results show that the classification accuracy of the hybrid model and the generalization ability is also improved [49]. Therefore, by leveraging the GEE platform and combining the strengths of both CNN and RF, we can fully capitalize on their advantages. In addition, MSIC-Otsu is a fully automatic met hod that can effectively extract the maximum water boundary of the lake to a certain extent, identify the potential area of aquatic vegetation distribution, thereby reducing the likelihood of missed measurements. Moreover, in the mapping process, there is no need for human intervention, training samples, or auxiliary information. Practice has proven that this method can efficiently and directly extract aquatic vegetation, overcoming the limitations of traditional methods such as fuzzy water boundaries, spectral mixing, and classification accuracy. In addition, during the vegetation extraction process, NDVI was less affected by turbid water signals, offering certain advantages in extracting submerged vegetation information. This improvement contributes to the accuracy and robustness of aquatic vegetation extraction. Therefore, the fusion of CNN and RF can effectively address the challenge of extracting aquatic vegetation, resulting in more reliable and accurate classification results.

In order to verify the effectiveness of CNN-RF, we compared it with the results extracted by Otsu, CNN, and RF. The classification was realized on the GEE platform, Otsu used an adaptive threshold to extract the results, and the decision tree value of RF was set to 100. We used PyTorch as a deep learning framework, CNN-RF and CNN had trained 200 epochs with a learning rate of 0.007, and the optimizer was sgd. The weight attenuation value was 0.0004, with a total of 1100 training samples and 100 test samples. The classification accuracy is shown in Table 4.

It is worth mentioning that CNN-RF outperforms other methods in classification accuracy. The Kappa coefficient of CNN-RF is 0.85, and OA is 0.91, which is higher than other classification methods. Then, taking Chagan Lake in 2020 as an example, we compare the enlarged images of the extraction results of different classification methods. As shown in Figure 11, CNN-RF is good at distinguishing aquatic vegetation/inland vegetation near water areas, providing clearer land cover boundaries and more concentrated distribution results. In contrast, RF needs further improvement in accurately separating aquatic vegetation from inland vegetation. The extraction result of CNN is inferior to that of CNN-RF,

and the accuracy of OA in extracting water is higher, but there is a lot of misclassification in the process of extracting aquatic vegetation and inland vegetation.

Table 4. Accuracy of different classification methods.

Land Use	Accuracy	Otsu	RF	CNN	CNN-RF
Aquatic vegetation	UA	0.75	0.88	0.89	0.91
	PA	0.82	0.89	0.91	0.89
Water	UA	0.91	0.91	0.91	0.91
	PA	0.94	0.91	0.91	0.94
Other	UA	0.75	0.86	0.89	0.90
	PA	0.62	0.83	0.86	0.90
	Kappa	0.68	0.81	0.84	0.85
	OA	0.80	0.88	0.90	0.91
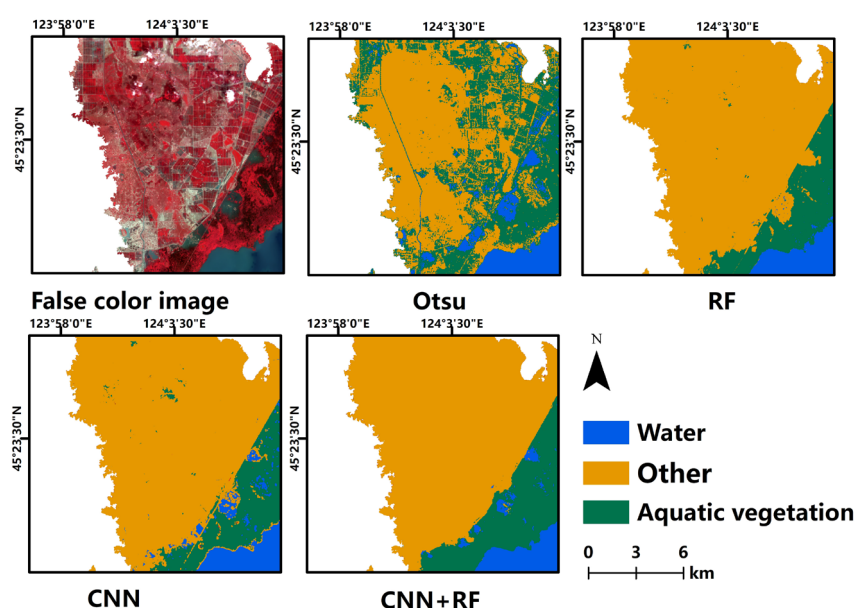
Figure 11. Classification maps of different classification methods.

4.2. Uncertainties in Aquatic Vegetation Mapping

In this study, we monitored the areal extents of aquatic vegetation over the past 36 years. However, due to the limited spatial resolution of Landsat series satellite data, there are challenges in identifying patches less than 30 m. Additionally, Landsat satellites have a relatively extended revisit period of 16 days, which may not capture short-term fluctuations in aquatic vegetation, especially during seasons characterized by rapid growth or decline. Moreover, we cannot guarantee that each pixel contains enough cloud-free observations to acquire key information about land cover after cloud masking. In situations where both algae blooms and aquatic vegetation are present in water, especially if the density of the algae bloom is low and the vegetation signal is weak, the NDVI value may become negative and omit the vegetation signal during the extraction process, potentially leading to misidentification with water. For example, from August to September 2017, there was a weak algal bloom in the middle and lower part of Hulun Lake, and the weak algal bloom did not produce obvious color change or texture characteristics, but this area was divided into water areas in this paper. Despite these uncertainties, the extraction of aquatic vegetation relies on consistent data sources and methods, encompassing long-term (36 years) multi-temporal information on aquatic vegetation and dynamics in the CARB.

5. Conclusions

In this study, we proposed a high-precision and robust classification method for extracting aquatic vegetation The CNN-RF classification method used in this paper has higher accuracy and can quickly process a large amount of data at one time, achieving efficient classification and greater robustness compared to CNN and RF alone. The basic idea involves employing an image composite to construct spatially and spectrally uniform images. We composed the maximum mNDWI index and extracted the water surface area using Otsu binary segmentation. Only lakes with an area larger than 20 km^2 were considered in this paper. The mask extracts the maximum NDVI composite image to identify potential aquatic vegetation areas. The resulting maximum NDVI composite image is then inputted into the CNN model to extract features. Subsequently, these features are fed into the RF classifier for accurate classification, enabling the precise mapping of the spatial and temporal distribution of aquatic vegetation from 1985 to 2020. According to the accuracy assessment, all the maps in the dataset exhibit high producer and user accuracy. Water surface and aquatic vegetation areas larger than 20 km^2 in the CARB show an overall decreasing trend from 1985 to 2020, reducing from 3575 km^2 and 745 km^2 to 3412 km^2 and 687 km^2, respectively. Among them, the water area of Hulun Lake exhibits a decreasing trend, while the water areas of Chagan Lake and Xiaoxingkai Lake are relatively stable. The water area of Lianhuan Lake exhibits an initial decrease and then increases. In terms of aquatic vegetation, the area in Lianhuan Lake remains relatively stable. However, in Hulun Lake, the aquatic vegetation area shows an initial increase, then decreases significantly, and then fluctuates and rises. Chagan Lake's aquatic vegetation area fluctuates and then rises slowly, and Xiaoxingkai Lake's aquatic vegetation area fluctuates and then continues to decline. The proposed method for aquatic vegetation information extraction in this paper not only extends the spatial portability of the model but also provides a powerful method and theoretical support for future extraction and monitoring of aquatic vegetation. The dataset of aquatic vegetation is invaluable for creating historical background maps of aquatic vegetation and evaluating the habitats of aquatic organisms, including their applicability to various species. In this study, an intriguing question emerges: can we further optimize the RF model to enhance interpretability when extracting aquatic vegetation from lakes using the CNN-RF approach? Additionally, future work will involve the development of a Landsat calibration model using high-resolution images. This calibration model aims to refine Landsat satellite-derived aquatic vegetation images, enabling a long-term series of fine classifications for various aquatic vegetation groups.

References

1. Yang, G.; Ma, R.; Zhang, L.; Jiang, J.; Yao, S.; Zhang, M.; Zeng, H.D. Lake Status, Major Problems and Protection Strategy in China. *J. Lake Sci.* **2010**, *22*, 799–810.
2. Parkes, M. Personal Commentaries on "Ecosystems and Human Well-Being: Health Synthesis—A Report of the Millennium Ecosystem Assessment". *EcoHealth* **2006**, *3*, 136–140. [CrossRef]
3. Inácio, M.; Barceló, D.; Zhao, W.; Pereira, P. Mapping Lake Ecosystem Services: A Systematic Review. *Sci. Total Environ.* **2022**, *847*, 157561. [CrossRef] [PubMed]
4. Jeppesen, E.; Søndergaard, M.; Søndergaard, M.; Christoffersen, K. *The Structuring Role of Submerged Macrophytes in Lakes*; Springer Science & Business Media: Berlin/Heidelberg, Germany, 2012; Volume 131, ISBN 1-4612-0695-2.
5. Horppila, J.; Nurminen, L. Effects of Submerged Macrophytes on Sediment Resuspension and Internal Phosphorus Loading in Lake Hiidenvesi (Southern Finland). *Water Res.* **2003**, *37*, 4468–4474. [CrossRef] [PubMed]
6. Jia, M.; Mao, D.; Wang, Z.; Ren, C.; Zhu, Q.; Li, X.; Zhang, Y. Tracking Long-Term Floodplain Wetland Changes: A Case Study in the China Side of the Amur River Basin. *Int. J. Appl. Earth Obs. Geoinf.* **2020**, *92*, 102185. [CrossRef]
7. Murphy, F.; Schmieder, K.; Baastrup-Spohr, L.; Pedersen, O.; Sand-Jensen, K. Five Decades of Dramatic Changes in Submerged Vegetation in Lake Constance. *Aquat. Bot.* **2018**, *144*, 31–37. [CrossRef]
8. Zhang, Y.; Liu, X.; Qin, B.; Shi, K.; Deng, J.; Zhou, Y. Aquatic Vegetation in Response to Increased Eutrophication and Degraded Light Climate in Eastern Lake Taihu: Implications for Lake Ecological Restoration. *Sci. Rep.* **2016**, *6*, 23867. [CrossRef] [PubMed]
9. Fourqurean, J.W.; Duarte, C.M.; Kennedy, H.; Marbà, N.; Holmer, M.; Mateo, M.A.; Apostolaki, E.T.; Kendrick, G.A.; Krause-Jensen, D.; McGlathery, K.J. Seagrass Ecosystems as a Globally Significant Carbon Stock. *Nat. Geosci.* **2012**, *5*, 505–509. [CrossRef]
10. Massicotte, P.; Bertolo, A.; Brodeur, P.; Hudon, C.; Mingelbier, M.; Magnan, P. Influence of the Aquatic Vegetation Landscape on Larval Fish Abundance. *J. Great Lakes Res.* **2015**, *41*, 873–880. [CrossRef]
11. Hilt, S.; Gross, E.M.; Hupfer, M.; Morscheid, H.; Mählmann, J.; Melzer, A.; Poltz, J.; Sandrock, S.; Scharf, E.-M.; Schneider, S. Restoration of Submerged Vegetation in Shallow Eutrophic Lakes–A Guideline and State of the Art in Germany. *Limnologica* **2006**, *36*, 155–171. [CrossRef]
12. Zeng, L.; He, F.; Dai, Z.; Xu, D.; Liu, B.; Zhou, Q.; Wu, Z. Effect of Submerged Macrophyte Restoration on Improving Aquatic Ecosystem in a Subtropical, Shallow Lake. *Ecol. Eng.* **2017**, *106*, 578–587. [CrossRef]
13. Luo, J.H.; Yang, J.Z.C.; Duan, H.T.; Lu, L.R.; Sun, Z.; Xin, Y.H. Research Progress of Aquatic Vegetation Remote Sensing in Shallow Lakes. *Natl. Remote Sens. Bull.* **2022**, *26*, 68–76.
14. Wen, K.; Gao, B.; Li, M. Quantifying the Impact of Future Climate Change on Runoff in the Amur River Basin Using a Distributed Hydrological Model and CMIP6 GCM Projections. *Atmosphere* **2021**, *12*, 1560. [CrossRef]
15. Wang, Z.; Song, K.; Ma, W.; Ren, C.; Zhang, B.; Liu, D.; Chen, J.M.; Song, C. Loss and Fragmentation of Marshes in the Sanjiang Plain, Northeast China, 1954–2005. *Wetlands* **2011**, *31*, 945–954. [CrossRef]
16. Mao, D.; Tian, Y.; Wang, Z.; Jia, M.; Du, J.; Song, C. Wetland Changes in the Amur River Basin: Differing Trends and Proximate Causes on the Chinese and Russian Sides. *J. Environ. Manag.* **2021**, *280*, 111670. [CrossRef] [PubMed]
17. Sokolova, G.V.; Verkhoturov, A.L.; Korolev, S.P. Impact of Deforestation on Streamflow in the Amur River Basin. *Geosciences* **2019**, *9*, 262. [CrossRef]
18. Han, D.; Gao, C.; Liu, H.; Yu, X.; Li, Y.; Cong, J.; Wang, G. Vegetation Dynamics and Its Response to Climate Change during the Past 2000 Years along the Amur River Basin, Northeast China. *Ecol. Indic.* **2020**, *117*, 106577. [CrossRef]
19. Zou, Y.; Wang, L.; Xue, Z.; Mingju, E.; Jiang, M.; Lu, X.; Yang, S.; Shen, X.; Liu, Z.; Sun, G. Impacts of Agricultural and Reclamation Practices on Wetlands in the Amur River Basin, Northeastern China. *Wetlands* **2018**, *38*, 383–389. [CrossRef]
20. Zhang, J.; Ma, K.; Fu, B. Wetland Loss under the Impact of Agricultural Development in the Sanjiang Plain, NE China. *Environ. Monit. Assess.* **2010**, *166*, 139–148. [CrossRef]
21. Bolpagni, R.; Bresciani, M.; Laini, A.; Pinardi, M.; Matta, E.; Ampe, E.M.; Giardino, C.; Viaroli, P.; Bartoli, M. Remote Sensing of Phytoplankton-Macrophyte Coexistence in Shallow Hypereutrophic Fluvial Lakes. *Hydrobiologia* **2014**, *737*, 67–76. [CrossRef]
22. Luo, J.; Ma, R.; Duan, H.; Hu, W.; Zhu, J.; Huang, W.; Lin, C. A New Method for Modifying Thresholds in the Classification of Tree Models for Mapping Aquatic Vegetation in Taihu Lake with Satellite Images. *Remote Sens.* **2014**, *6*, 7442–7462. [CrossRef]
23. Jing, R.; Deng, L.; Zhao, W.J.; Gong, Z.N. Object-Oriented Aquatic Vegetation Extracting Approach Based on Visible Vegetation Indices. *Ying Yong Sheng Tai Xue Bao J. Appl. Ecol.* **2016**, *27*, 1427–1436.
24. Chen, Q.; Yu, R.; Hao, Y.; Wu, L.; Zhang, W.; Zhang, Q.; Bu, X. A New Method for Mapping Aquatic Vegetation Especially Underwater Vegetation in Lake Ulansuhai Using GF-1 Satellite Data. *Remote Sens.* **2018**, *10*, 1279. [CrossRef]
25. Wang, H.; Li, Y.; Zeng, S.; Cai, X.; Bi, S.; Liu, H.; Mu, M.; Dong, X.; Li, J.; Xu, J. Recognition of Aquatic Vegetation above Water Using Shortwave Infrared Baseline and Phenological Features. *Ecol. Indic.* **2022**, *136*, 108607. [CrossRef]
26. Ashford, P. Field Methods and Photogrammetric Techniques for Mapping Aquatic Vegetation Using Unmanned Aerial Systems. Master's Thesis, University of Georgia, Athens, GA, USA, 2019.
27. Yuan, Q.; Shen, H.; Li, T.; Li, Z.; Li, S.; Jiang, Y.; Xu, H.; Tan, W.; Yang, Q.; Wang, J. Deep Learning in Environmental Remote Sensing: Achievements and Challenges. *Remote Sens. Environ.* **2020**, *241*, 111716. [CrossRef]
28. Li, B.; Yang, G.; Wan, R.; Dai, X.; Zhang, Y. Comparison of Random Forests and Other Statistical Methods for the Prediction of Lake Water Level: A Case Study of the Poyang Lake in China. *Hydrol. Res.* **2016**, *47*, 69–83. [CrossRef]

29. Zhao, C.; Jia, M.; Wang, Z.; Mao, D.; Wang, Y. Toward a Better Understanding of Coastal Salt Marsh Mapping: A Case from China Using Dual-Temporal Images. *Remote Sens. Environ.* **2023**, *295*, 113664. [CrossRef]

30. Ji, M.; Liu, L.; Du, R.; Buchroithner, M.F. A Comparative Study of Texture and Convolutional Neural Network Features for Detecting Collapsed Buildings after Earthquakes Using Pre-and Post-Event Satellite Imagery. *Remote Sens.* **2019**, *11*, 1202. [CrossRef]

31. Otsu, N. A Threshold Selection Method from Gray-Level Histograms. *IEEE Trans. Syst. Man Cybern.* **1979**, *9*, 62–66. [CrossRef]

32. Wang, Z.H.; Xin, C.L.; Sun, Z.; Luo, J.H.; Ma, R.H. Automatic Extraction Method of Aquatic Vegetation Types in Small Shallow Lakes Based on Sentinel-2 Data: A Case Study of Cuiping Lake. *Remote Sens. Inf* **2019**, *34*, 132–141.

33. Rouse, J.W., Jr.; Haas, R.H.; Deering, D.W.; Schell, J.A.; Harlan, J.C. *Monitoring the Vernal Advancement and Retrogradation (Green Wave Effect) of Natural Vegetation*; NASA: Washington, DC, USA, 1974.

34. Duan, Y.; Li, X.; Zhang, L.; Chen, D.; Ji, H. Mapping National-Scale Aquaculture Ponds Based on the Google Earth Engine in the Chinese Coastal Zone. *Aquaculture* **2020**, *520*, 734666. [CrossRef]

35. Jia, M.; Wang, Z.; Mao, D.; Ren, C.; Wang, C.; Wang, Y. Rapid, Robust, and Automated Mapping of Tidal Flats in China Using Time Series Sentinel-2 Images and Google Earth Engine. *Remote Sens. Environ.* **2021**, *255*, 112285. [CrossRef]

36. Simis, S.G.; Peters, S.W.; Gons, H.J. Remote Sensing of the Cyanobacterial Pigment Phycocyanin in Turbid Inland Water. *Limnol. Oceanogr.* **2005**, *50*, 237–245. [CrossRef]

37. LeCun, Y.; Bottou, L.; Bengio, Y.; Haffner, P. Gradient-Based Learning Applied to Document Recognition. *Proc. IEEE* **1998**, *86*, 2278–2324. [CrossRef]

38. Chen, L.-C.; Zhu, Y.; Papandreou, G.; Schroff, F.; Adam, H. Encoder-Decoder with Atrous Separable Convolution for Semantic Image Segmentation. *arXiv* **2018**, arXiv:1802.02611.

39. Rodriguez-Galiano, V.F.; Ghimire, B.; Rogan, J.; Chica-Olmo, M.; Rigol-Sanchez, J.P. An Assessment of the Effectiveness of a Random Forest Classifier for Land-Cover Classification. *ISPRS J. Photogramm. Remote Sens.* **2012**, *67*, 93–104. [CrossRef]

40. Parmar, A.; Katariya, R.; Patel, V. A Review on Random Forest: An Ensemble Classifier. In Proceedings of the International Conference on Intelligent Data Communication Technologies and Internet of Things (ICICI) 2018, Coimbatore, India, 7–8 August 2018; Springer: Cham, Switzerland, 2019; pp. 758–763.

41. Liaw, A.; Wiener, M. Classification and Regression by randomForest. *R News* **2002**, *2*, 18–22.

42. Sun, T.; Liu, M.; Ye, H.; Yeung, D.-Y. Point-Cloud-Based Place Recognition Using CNN Feature Extraction. *IEEE Sens. J.* **2019**, *19*, 12175–12186. [CrossRef]

43. Zhang, M.; Li, W.; Du, Q. Diverse Region-Based CNN for Hyperspectral Image Classification. *IEEE Trans. Image Process.* **2018**, *27*, 2623–2634. [CrossRef]

44. Zeiler, M.D.; Fergus, R. Visualizing and Understanding Convolutional Networks. In Proceedings of the Computer Vision–ECCV 2014: 13th European Conference, Zurich, Switzerland, 6–12 September 2014; Proceedings, Part I 13. Springer: Cham, Switzerland, 2014; pp. 818–833.

45. Li, M.; Wang, L.; Wang, J.; Li, X.; She, J. Comparison of Land Use Classification Based on Convolutional Neural Network. *J. Appl. Remote Sens.* **2020**, *14*, 016501. [CrossRef]

46. Ståhl, N.; Weimann, L. Identifying Wetland Areas in Historical Maps Using Deep Convolutional Neural Networks. *Ecol. Inform.* **2022**, *68*, 101557. [CrossRef]

47. Freund, Y.; Schapire, R.E. A Decision-Theoretic Generalization of on-Line Learning and an Application to Boosting. *J. Comput. Syst. Sci.* **1997**, *55*, 119–139. [CrossRef]

48. Breiman, L. Bagging Predictors. *Mach. Learn.* **1996**, *24*, 123–140. [CrossRef]

49. Xi, E. Image Classification and Recognition Based on Deep Learning and Random Forest Algorithm. *Wirel. Commun. Mob. Comput.* **2022**, *2022*, 2013181. [CrossRef]